

# In Situ Observation of $\beta$ -Ga<sub>2</sub>O<sub>3</sub> Schottky Diode Failure Under Forward Biasing Condition

Zahabul Islam, Minghan Xian, Aman Haque<sup>ID</sup>, Fan Ren, *Fellow, IEEE*,  
Marko Tadjer<sup>ID</sup>, *Senior Member, IEEE*, Nicholas Glavin,  
and Stephen Pearton

**Abstract**—In this article, we investigate defect nucleation leading to device degradation in  $\beta$ -Ga<sub>2</sub>O<sub>3</sub> Schottky barrier diodes by operating them inside a transmission electron microscope. Such *in situ* approach allows simultaneous visualization and quantitative device characterization, not possible with the current art of postmortem microscopy. High current density and associated mechanical and thermal fields are shown to induce different types of crystal defects, from vacancy cluster and stacking fault to micro-crack generation prior to failure. These structural defects can act as traps for carrier and cause device failure at high biasing voltage. Fundamental insights on nucleation of these defects and their evolution are important from materials reliability and device design perspectives.

**Index Terms**— $\beta$ -Ga<sub>2</sub>O<sub>3</sub>, crystal defects, *in situ* transmission electron microscope (TEM), Schottky barrier diodes (SBDs).

## I. INTRODUCTION

HIGH breakdown field of wide bandgap materials makes them well-suited to high power electronics applications [1]–[3]. Both GaN and SiC are commercialized for power switching and control systems, while materials with

even larger bandgaps, such as diamond, high-Al AlGaN, and Ga<sub>2</sub>O<sub>3</sub>, are attracting significant interest for achieving even higher performance levels. In particular, the beta-polytype of Ga<sub>2</sub>O<sub>3</sub> is an attractive material because of its low cost, bulk growth methods, wide bandgap of 4.8–4.9 eV, and high breakdown field ( $\sim 8$  MV/cm) [4]–[7]. Ga<sub>2</sub>O<sub>3</sub> has three times higher breakdown field strength compared to GaN and 4H-SiC [7] and possesses one order of magnitude and three times higher Baliga's figure of merit (BFOM) compared to 4H-SiC and GaN, respectively, [4], [5]. These exceptional properties make Ga<sub>2</sub>O<sub>3</sub> a suitable material for next-generation high power electronics such as Schottky barrier diodes (SBDs) and MOSFETs with low loss, high breakdown field, and high voltage switching capability [4], [5], [8]–[21].

SBDs are a particular device concept that exhibit low ON-state loss, short recovery time, low ON-resistance, and high switching speeds [4], [5], [8], [9], [12], [22]–[24]. A large number of studies [8], [9], [12] have shown very promising performance from  $\beta$ -Ga<sub>2</sub>O<sub>3</sub> SBDs, with breakdown voltages over 2 kV and forward currents  $>30$  A from large area devices. The electrical behavior of SBDs can be affected by the choice of Schottky metal contact, and the presence of interface states [25]–[31]. Crystal defects can also affect the performance of the SBDs and contribute to high leakage current [28].

Large area vertical geometry  $\beta$ -Ga<sub>2</sub>O<sub>3</sub> SBDs are potential candidates for high power switching application [32]. Initial studies show the failure modes of  $\beta$ -Ga<sub>2</sub>O<sub>3</sub> SBDs under forward and reverse bias conditions are different [5], [32]. The reverse bias failure mode is governed by the pit formation at the edge of the Schottky contact where the electric field strength is highest, whereas forward bias failure mode shows contact area and device layer cracking and in some cases, delamination of epitaxial layers from the underlying substrate [32]. Temperature-dependent electrical characterization of  $\beta$ -Ga<sub>2</sub>O<sub>3</sub> SBD shows that the Schottky barrier height (SBH) can be affected by the device operating temperature [26], [27], [32]–[35], which is reflected by their current–voltage ( $I$ – $V$ ) characteristics. Relatively less is known about the fundamental mechanisms behind the evolution of damage and ultimately, failure of these devices. The majority of the studies extrapolate the failure mechanisms with either “signature” failure pattern in the device characteristics data [36]–[38] or with postfailure analysis of the device. Only

Manuscript received March 26, 2020; revised May 13, 2020; accepted June 2, 2020. Date of publication June 19, 2020; date of current version July 23, 2020. The work of Zahabul Islam and Aman Haque was supported by the National Science Foundation, USA, through the Civil, Mechanical and Manufacturing Innovation (CMMI) Nanomanufacturing under Grant 1760931. The work of Minghan Xian, Fan Ren, and Stephen Pearton was supported in part by HDTRA1-17-1-0011 (Jacob Calkins, monitor) and in part by NSF under Grant DMR 1856662 (Tania Paskova). The work of Marko Tadjer was supported by the Office of Naval Research (ONR). The work of Nicholas Glavin was supported by the Air Force Office of Scientific Research under Grant FA9550-19RYCOR050. The review of this article was arranged by Editor S. Chowdhury. (Corresponding author: Aman Haque.)

Zahabul Islam and Aman Haque are with the Department of Mechanical Engineering, Pennsylvania State University, University Park, PA 16802 USA (e-mail: mqj5074@psu.edu; mah37@psu.edu).

Minghan Xian and Fan Ren are with the Department of Chemical Engineering, University of Florida, Gainesville, FL 32611 USA (e-mail: mxian@ufl.edu; fren@che.ufl.edu).

Marko Tadjer is with the U.S. Naval Research Laboratory, Washington, DC 20375 USA (e-mail: marko.tadjer@nrl.navy.mil).

Nicholas Glavin is with the Air Force Research Laboratory, Wright-Patterson AFB, OH 45433 USA (e-mail: nicholas.glavin.1@us.af.mil).

Stephen Pearton is with the Department of Materials Science and Engineering, University of Florida, Gainesville, FL 32611 USA (e-mail: spear@ufl.edu).

Color versions of one or more of the figures in this article are available online at <http://ieeexplore.ieee.org>.

Digital Object Identifier 10.1109/TED.2020.3000441

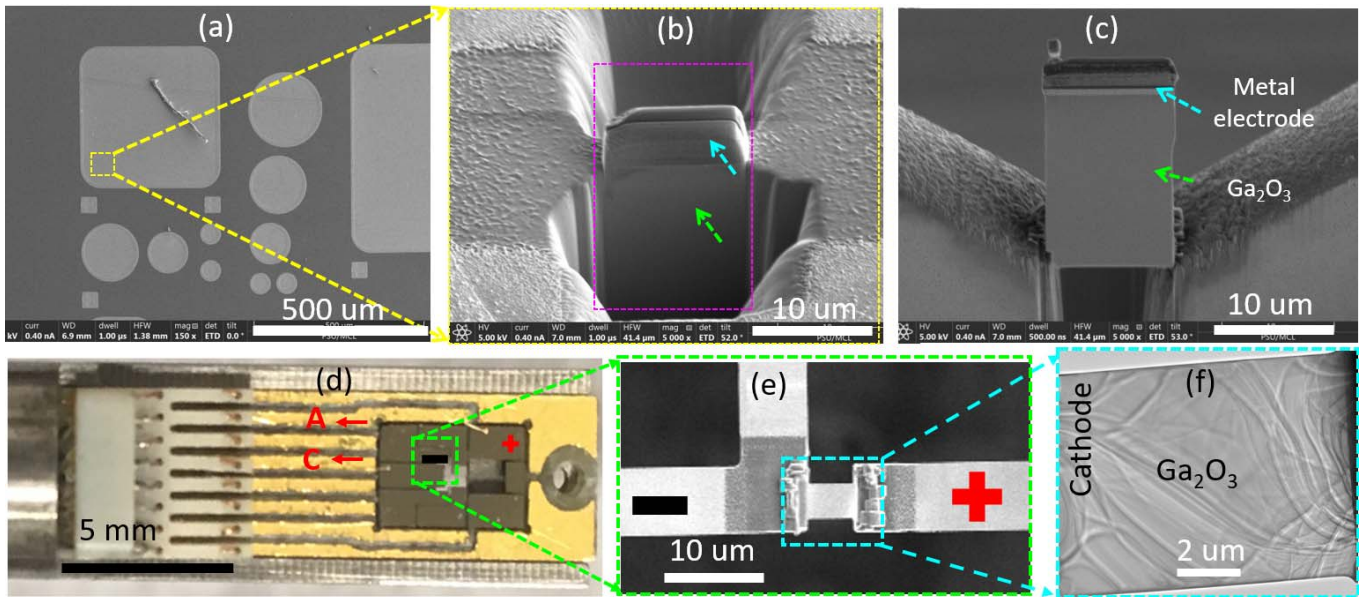


**Fig. 1.** (a) SEM micrograph of bulk Ga<sub>2</sub>O<sub>3</sub> SBD. (b) Coupon preparation from the bulk SBD device. (c) TEM cross section of the thin film SBD before mounting on the MEMS device. (d) MEMS chip on a TEM holder for *in situ* biasing. (e) Electron transparent sample mounted on the MEMS device. (f) Low magnification TEM BF image of  $\beta$ -Ga<sub>2</sub>O<sub>3</sub> SBD.

a few recent studies [39]–[41] have attempted to investigate the failure mode of electronic devices under real-time operating condition. However, such *in situ* or in operando experiments have not been extended to Ga<sub>2</sub>O<sub>3</sub> SBDs yet.

In our present study, we demonstrate an *in situ* experimental philosophy that allows us to investigate  $\beta$ -Ga<sub>2</sub>O<sub>3</sub> SBDs failure under forward biasing condition inside a transmission electron microscope (TEM). The uniqueness of the study is that it allows us for the simultaneous visualization of the microstructure and quantitative characterization during the SBD device operation. We prepared electron transparent functional specimen from a bulk  $\beta$ -Ga<sub>2</sub>O<sub>3</sub> Schottky diode using a focused ion beam (FIB). The specimen was mounted and wire-bonded on customized *in situ* TEM chip to perform experiments. Real-time visualization at high-resolution imaging accompanied by energy-dispersive X-ray spectroscopy (EDS), high-angle annular dark-field (HAADF) imaging, and selected area electron diffraction pattern were performed to characterize the microstructure and chemistry. The assortment of device characteristics, microstructure, and elemental diffusion data is expected to provide useful insights into the failure mechanism of  $\beta$ -Ga<sub>2</sub>O<sub>3</sub> SBDs and design guidelines.

## II. EXPERIMENTAL SECTION

The device structure and fabrication have been described in detail previously [14]. Briefly, the field-plated, edge-terminated vertical Schottky diodes were fabricated on a 20-μm-thick Si-doped n-type Ga<sub>2</sub>O<sub>3</sub> drift layer grown on 650-μm thick  $\beta$ -Ga<sub>2</sub>O<sub>3</sub> substrate using halide vapor phase epitaxy (HVPE). The  $\beta$ -Ga<sub>2</sub>O<sub>3</sub> substrate was an Sn-doped  $\beta$ -Ga<sub>2</sub>O<sub>3</sub> single crystal wafer with (001) surface orientation grown by the edge-defined film-fed method with a carrier concentration of  $3.6 \times 10^{18} \text{ cm}^{-3}$ . A backside Ohmic contact was formed with electron-beam-deposited Ti/Au fol-

lowed by rapid thermal annealing at 550 °C for 30 s in N<sub>2</sub>. Next, 40 nm of SiO<sub>2</sub> and 360 nm of SiN<sub>x</sub> were deposited as dielectric layers. Dielectric contact windows were opened with buffered oxide etchant (BOE). E-beam-evaporated Ni/Au (80 nm/420 nm) metallization was used for the Schottky contacts, which overlapped the dielectric windows by 10 μm.

Electron transparent (nominally 100-nm thick)  $\beta$ -Ga<sub>2</sub>O<sub>3</sub> coupons were prepared and lifted out from the SBD [Fig. 1(a)] using a Ga<sup>+</sup> FIB [Fig. 1(b)] in a Helios Nanolab DualBeam scanning electron microscope (SEM). This involved three important steps: 1) 100-nm thin sample preparation, 2) transfer of 100-nm thin sample on microelectromechanical system (MEMS) device [Fig. 1(e)] [39], [40], and 3) wire bonding of MEMS device [42] on a TEM chip carrier [Fig. 1(d)]. At first, a coupon was lifted out from the bulk  $\beta$ -Ga<sub>2</sub>O<sub>3</sub> SBDs and attached on a copper TEM grid [Fig. 1(c)] which was further thinned down to 100-nm electron transparent sample [Fig. 1(f)] using Ga<sup>+</sup> FIB. Thinning down of the coupon involves a series of ion beam accelerating voltages and a wide range of current steps 21 nA–72 pA. The thickness of the sample was monitored at regular intervals during the thinning down process, and both accelerating voltage and currents were adjusted depending on the sample thickness. The second-step sample preparation uses low accelerating voltage to transfer the sample from TEM copper grid to the MEMS device. Low, i.e., 5-kV accelerating voltage-transfer steps were chosen to avoid any beam damage and redeposition. Electrical connections [Fig. 1(e)] were made using FIB-deposited platinum. Fig. 1(e) shows the transferred sample on the MEMS device, which is further mounted on an *in situ* TEM holder [Fig. 1(d)]. Electrical characterization was performed inside a field emission 200-kV FEI Talos F200X TEM equipped with energy dispersive spectroscopy (EDS) with 1.2-Å resolution.



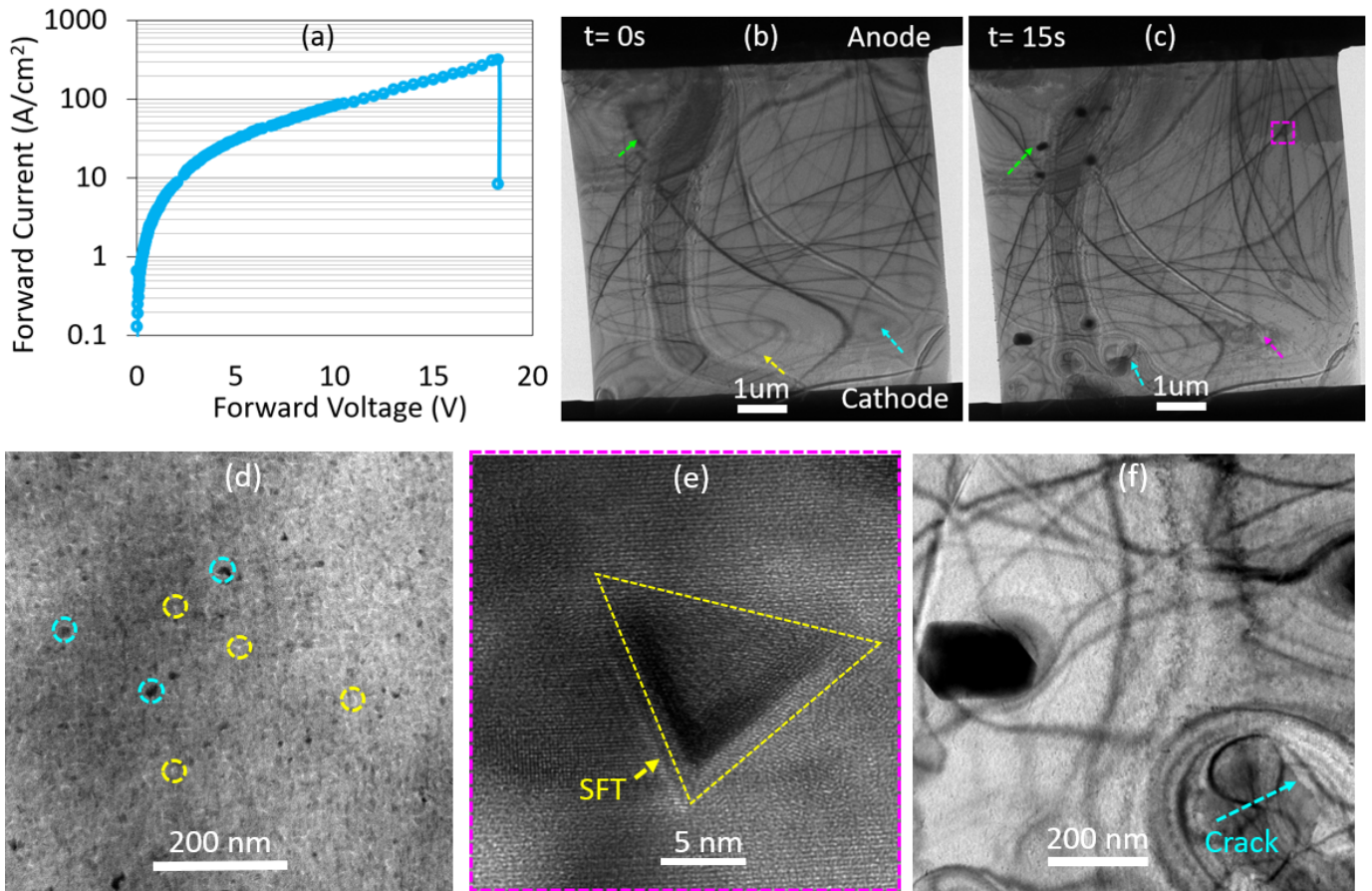


Fig. 2. (a)  $I$ - $V$  characteristics under forward biasing condition. TEM BF images during failure at time (b)  $t = 0$  s and (c)  $t = 15$  s. Structural transformation in the  $\beta$ -Ga<sub>2</sub>O<sub>3</sub> layer after failure. (d) TEM BF image of vacancy clusters. (e) HRTEM images of SFT [corresponds to the pink color region in (c)]. (f) Defects near the cathode area.

### III. RESULTS AND DISCUSSION

The  $11 \mu\text{m} \times 7 \mu\text{m} \times 100\text{-nm}$  electron transparent  $\beta$ -Ga<sub>2</sub>O<sub>3</sub>SBDs [Fig. 1(f)] were tested under accelerated forward biasing conditions. During the experiment, we gradually increased the forward bias at an interval of 20 mV until the device fails. Each biasing step was followed by a 1-min delay for relaxation, at which point the system was stable both mechanically and electrically. Fig. 2(a) shows the SBD current-voltage ( $I$ - $V$ ) characteristics under forward biasing condition. Low magnification TEM bright field (BF) images [Figs. 1(f) and 2(b) and (c)] show bend contours which arise from elastic bending during specimen preparation. Fig. 2(b) and (c) shows the TEM BF images to capture microstructural changes during operation. The calculated current density prior to the failure is  $3.2 \times 10^2 \text{ A/cm}^2$ , which is in well agreement with the reported [5], [30] value. This high current density is enough to introduce thermal stress in the device which could further initiate microstructural changes at the anode and cathode areas, as shown in Fig. 2(b) and (c). High-resolution TEM (HRTEM) images [Fig. 2(d)–(f)] indicate generation of severe crystal defects, such as vacancy clusters, [Fig. 2(d)] amorphization, stacking fault tetrahedron (SFT), and crack [Fig. 2(f)] formation in the device layers.

As shown in Fig. 2(e) SFT is a pyramidal shape vacancy defect, and it may appear as a triangular shape in the TEM BF image [43]. SFT defects are an obvious indication of vacancy

generation in the device layer under high current density as shown in Fig. 2(e). These vacancies further accumulate to form SFT defects [44]. Similar types of stacking fault defects in Ga<sub>2</sub>O<sub>3</sub> have been reported recently [45]. During the failure both metal pool (green color dotted lines) and discernable cracks (cyan color dotted lines) formed in the device layer near the cathode as shown in Fig. 2(f). High current density accompanied by the thermal field could induce a sufficient amount of thermal stress in the device layer and initiate this mechanical cracking [9]. These structural defects might act as carrier traps and further accelerates device degradation.

During forward biasing, defects could generate near the anode area due to high current density in the SBD device (Fig. 3). Fig. 3 shows such defects evolution during forward biasing. The pink color arrowhead indicates the direction of the anode location. Before forward biasing, there was no obvious indication of crystal defects, as shown in Fig. 3(a). However, at 4.8 V, crystal defects start to appear as indicated by green circular regions in Fig. 3(b). These defects near the anode could affect SBH at the interface [22], which could affect forward output current. At this point calculated current density is  $2.9 \times 10^1 \text{ A/cm}^2$ , which can facilitate the development of thermal stress due to the Joule heating, and further contributes to the crystal defects evolution. The electrical field required to initiate crystal defects is approximately 0.5 MV/cm, this

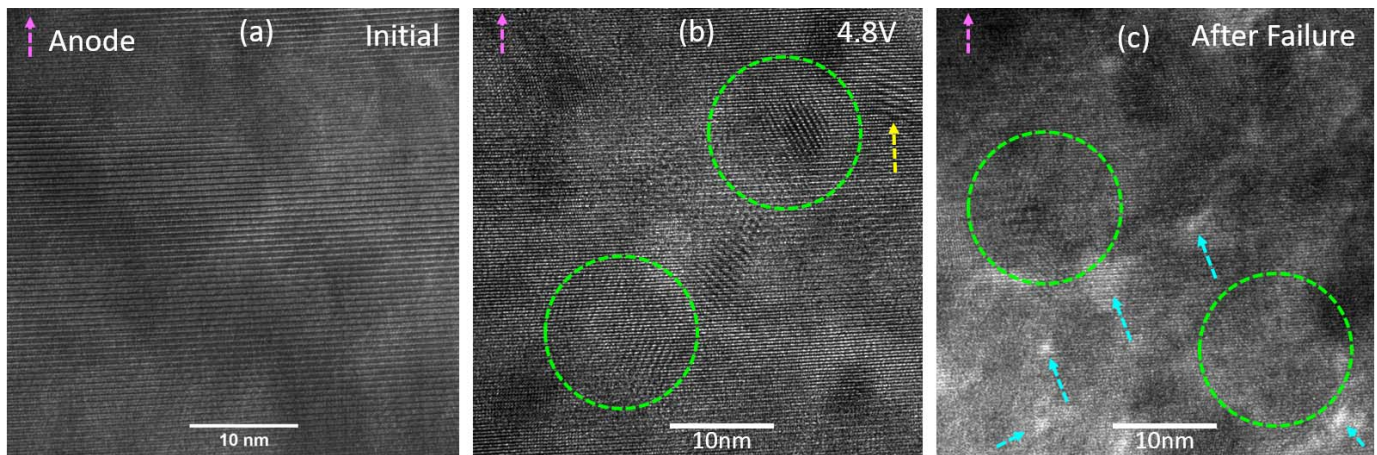


Fig. 3. HRTEM images near the anode area at different biasing conditions. (a) Initial condition, i.e., 0 V. (b) 4.8 V. (c) After failure.

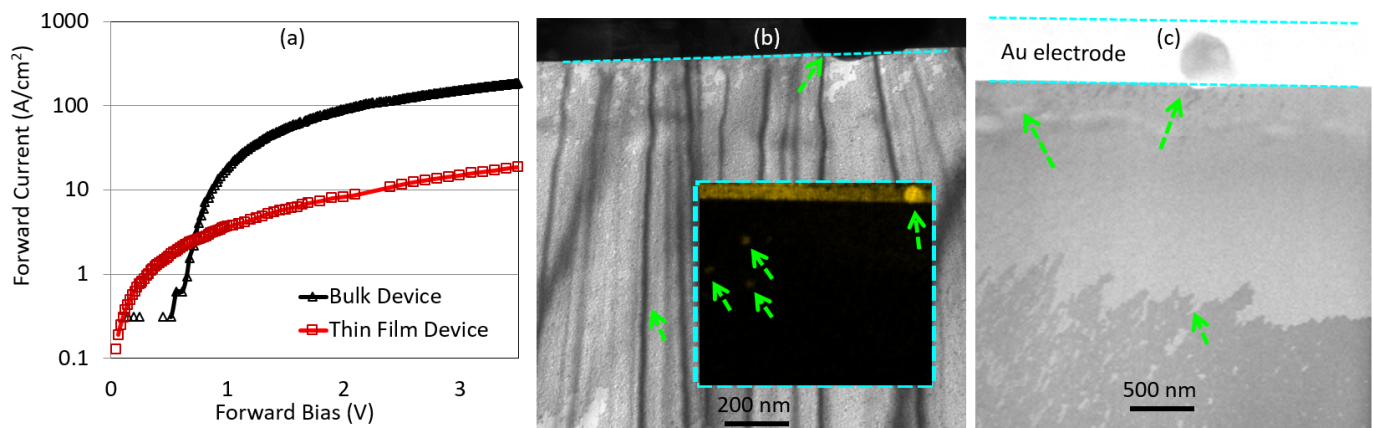


Fig. 4. (a) Comparison of output current between as-fabricated bulk device and thin film device. (b) BF TEM image shows gold diffusion in the channel layer. (c) Gold diffusion in the device layer captured by STEM image.

value is close to the experimental breakdown field strength approximately 0.54 MV/cm [46]. However, as we continue to increase forward biasing, the device fails by forming a vacancy-enriched area, as indicated by cyan color dotted arrowhead in Fig. 3(c). We also notice disruption in crystal structure and formation of small crystallites, as shown by green color dotted circles. This observation indicates that single-crystal Ga<sub>2</sub>O<sub>3</sub> disintegrates into a polycrystalline structure due to the thermo-mechanical field, which can significantly affect the device performance. In our present study, we notice that after failure the device behaves as an open circuit, and no significant current flow was measured through the device after this failure.

We have also compared forward output current obtained from as-fabricated bulk Ga<sub>2</sub>O<sub>3</sub> and electron transparent thin film device as shown in Fig. 4(a). Output current follows the similar  $I$ - $V$  characteristics; however, the magnitude of current density is slightly different which could be attributed to the thin film device geometry. Rigorous experimentation and modeling are required to mitigate this discrepancy and we left this issue for future study. Scanning transmission electron microscope (STEM) equipped with EDS allows us to identify individual elements in the device layer during the

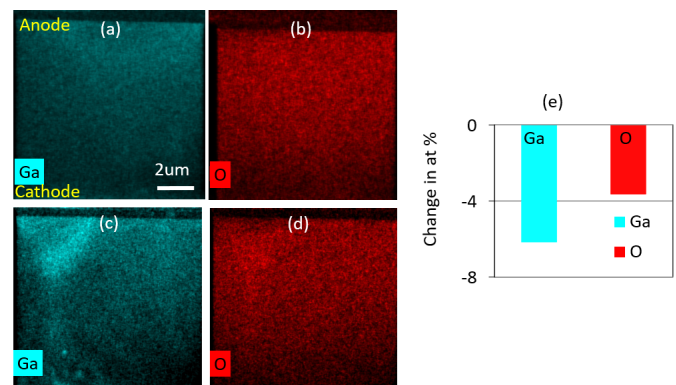


Fig. 5. EDS mapping of chemical elements (a) and (b) before biasing and (c) and (d) after failure. (e) Change in the atom percentage of individual chemical elements.

experiment. The chemical mapping provides insights into the diffusion of elements toward degradation of the SBD device during forward biasing. In our present study, we scan two EDS maps before and after the failure of the device, as shown in Fig. 5(a)–(d). On the EDS map, cyan and red colors represent gallium (Ga) and oxygen (O) atoms, respectively.



No discernable defects/abrupt changes in the elemental map are observed in the sample before biasing [Fig. 5(a) and (b)]. However, after failure, we observe the accumulation of Ga and O near the left side of the anode [Fig. 5(c) and (d)]. At the same time, we also identify the loss of Ga and O atoms from the cathode area of the device, which could be attributed to the Ga pool formation near the cathode area [Fig. 5(c)]. We also notice both Ga and O atoms migrate toward the anode area, which could be attributed to the thermo-migration of these atoms under the combined thermo-mechanical field at high current density. The unique geometry of the thin film SBD could introduce a nonuniform temperature profile along the thin film SBD due to the Joule heating. Thus, this thermal gradient in the sample might generate a nonuniform Ga profile in the thin film SBD device. Under high current density, the anode metal could degrade (as shown by the green dotted arrow in Fig. 4(b) and (c)). BF TEM image, EDS map [inset in Fig. 4(b)], and STEM images [Fig. 4(c)] show electrode metals diffusion in the channel layer at higher current density due to the high thermal field. This electrode degradation might significantly damage the interface layer and introduce the Schottky barrier inhomogeneity at the interface [23]. Hence, the device deviates from the ideal behavior.

STEM image and EDS mapping allow us to probe both structural and chemical transformation. For example, metal pool formation is confirmed by Fig. 5(c). However, without EDS mapping no elemental information could be extracted. The presence of a metallic pool of Ga near the cathode indicates a sufficiently high thermal field that may arise during the device operation and could transform  $\text{Ga}_2\text{O}_3$  to Ga atoms. Fig. 5(e) represents the relative weight percentage of Ga and O atoms after failure. Weight percentage loss of Ga and O atoms is approximately 6% and 4%, respectively, [Fig. 5(e)], which supports the device layer degradation and decomposition of  $\beta\text{-Ga}_2\text{O}_3$  at high current density.

Our present study reveals that high current density accompanied by the thermal field could induce a significant number of structural defects such as vacancy clusters, stacking faults, and cracking in the devices. These structural defects further act as carrier traps and might increase resistance to the current flow during the operation [24]. Observation indicates that failure mode could be attributed to the high thermo-mechanical field that may arise during the operation of the SBDs device. *In situ* TEM techniques have been already implemented to investigate both “ON-” [47] and “OFF-” [39] state failure study of high electron mobility transistor. Though our present study investigates forward biasing condition, however, a similar technique could be extended to study the reverse biasing failure mode. Further work is needed to correlate the scaling physics of the electron transparent device and the effects of specimen preparation before the findings can be applied to bulk SBDs.

#### IV. CONCLUSION

We demonstrated a new experimental direction in electron device reliability by operating an electron transparent  $\beta\text{-Ga}_2\text{O}_3$  SBD inside a TEM. The electrical measurements

and microscopy indicate that high current density could induce a significant concentration of crystal defects both in the electrode and device layer, which in turn increase series resistance. At high current density, the electrode metal can degrade, thus introducing inhomogeneous Schottky contact at the metal–semiconductor interface. Additionally, high current density-induced point defects can act as carrier traps, which significantly affect the electrical performance of the device. Metallic pool formation during the failure of the device indicates temperature plays a dominant role in the device failure. Furthermore, EDS mapping indicates the reduction of Ga and O atoms near the cathode area could be attributed to the migration of atoms under high current density. We conclude that the existing literature considers only postfailure analysis to predict the failure modes, whereas this article probed defects evolution and failure modes during real-time operation. Continuation of this article will provide invaluable insights on SBD device design and failure mechanism in the future.

#### REFERENCES

- [1] A. Q. Huang, “Power semiconductor devices for smart grid and renewable energy systems,” *Proc. IEEE*, vol. 105, no. 11, pp. 2019–2047, Nov. 2017.
- [2] A. Merkert, T. Krone, and A. Mertens, “Characterization and scalable modeling of power semiconductors for optimized design of traction inverters with Si- and SiC-devices,” *IEEE Trans. Power Electron.*, vol. 29, no. 5, pp. 2238–2245, May 2014.
- [3] J. Wang, V. Veliadis, J. Zhang, Y. Alsmadi, P. R. Wilson, and M. J. Scott, “IEEE ITRW working group position paper-system integration and application: Silicon carbide: A roadmap for silicon carbide adoption in power conversion applications,” *IEEE Power Electron. Mag.*, vol. 5, no. 2, pp. 40–44, Jun. 2018.
- [4] M. Higashiwaki *et al.*, “Recent progress in  $\text{Ga}_2\text{O}_3$  power devices,” *Semicond. Sci. Technol.*, vol. 31, no. 3, Mar. 2016, Art. no. 034001.
- [5] J. Yang, F. Ren, S. J. Pearton, and A. Kuramata, “Vertical geometry, 2-A forward current  $\text{Ga}_2\text{O}_3$  Schottky rectifiers on bulk  $\text{Ga}_2\text{O}_3$  substrates,” *IEEE Trans. Electron Devices*, vol. 65, no. 7, pp. 2790–2796, Jul. 2018.
- [6] S. B. Reese, T. Remo, J. Green, and A. Zakutayev, “How much will gallium oxide power electronics cost?” *Joule*, vol. 3, no. 4, pp. 903–907, Apr. 2019.
- [7] M. Higashiwaki and G. H. Jessen, “Guest editorial: The dawn of gallium oxide microelectronics,” *Appl. Phys. Lett.*, vol. 112, no. 6, Feb. 2018, Art. no. 060401.
- [8] J. Yang, S. Ahn, F. Ren, S. J. Pearton, S. Jang, and A. Kuramata, “High breakdown voltage (-201)  $\beta\text{-Ga}_2\text{O}_3$  Schottky rectifiers,” *IEEE Electron Device Lett.*, vol. 38, no. 7, pp. 906–909, Jul. 2017.
- [9] J. C. Yang, F. Ren, M. Tadjer, S. J. Pearton, and A. Kuramata, “2300V reverse breakdown voltage  $\text{Ga}_2\text{O}_3$  schottky rectifiers,” *ECS J. Solid State Sci. Technol.*, vol. 7, no. 5, pp. Q92–Q96, 2018.
- [10] Z. Hu *et al.*, “Breakdown mechanism in 1  $\text{kA}/\text{cm}^2$  and 960 V E-mode  $\beta\text{-Ga}_2\text{O}_3$  vertical transistors,” *Appl. Phys. Lett.*, vol. 113, no. 12, 2018, Art. no. 122103.
- [11] J. Yang *et al.*, “Vertical geometry 33.2 A, 4.8 MW  $\text{cm}^2$   $\text{Ga}_2\text{O}_3$  field-plated Schottky rectifier arrays,” *Appl. Phys. Lett.*, vol. 114, no. 23, Jun. 2019, Art. no. 232106.
- [12] W. Li *et al.*, “2.44 kV  $\text{Ga}_2\text{O}_3$  vertical trench Schottky barrier diodes with very low reverse leakage current,” in *IEDM Tech. Dig.*, Dec. 2018, pp. 5–8.
- [13] H. Dong *et al.*, “Fast switching  $\beta\text{-Ga}_2\text{O}_3$  power MOSFET with a trench-gate structure,” *IEEE Electron Device Lett.*, vol. 40, no. 9, pp. 1385–1388, Sep. 2019.
- [14] S. J. Pearton, F. Ren, M. Tadjer, and J. Kim, “Perspective:  $\text{Ga}_2\text{O}_3$  for ultra-high power rectifiers and MOSFETs,” *J. Appl. Phys.*, vol. 124, no. 22, 2018, Art. no. 220901.
- [15] M. Higashiwaki *et al.*, “Depletion-mode  $\text{Ga}_2\text{O}_3$  MOSFETs,” in *Proc. 71st Device Res. Conf.*, 2013, pp. 1–2.
- [16] M. H. Wong *et al.*, “First demonstration of vertical  $\text{Ga}_2\text{O}_3$  MOSFET: Planar structure with a current aperture,” in *Proc. 75th Annu. Device Res. Conf. (DRC)*, Jun. 2017, pp. 1–2.

- [17] A. J. Green *et al.*, " $\beta$ -Ga<sub>2</sub>O<sub>3</sub> MOSFETs for radio frequency operation," *IEEE Electron Device Lett.*, vol. 38, no. 6, pp. 790–793, Jun. 2017.
- [18] K. D. Chabak *et al.*, "Enhancement-mode Ga<sub>2</sub>O<sub>3</sub> wrap-gate fin field-effect transistors on native (100)  $\beta$ -Ga<sub>2</sub>O<sub>3</sub> substrate with high breakdown voltage," *Appl. Phys. Lett.*, vol. 109, no. 21, Nov. 2016, Art. no. 213501.
- [19] K. Zeng, A. Vaidya, and U. Singiseti, "710 V breakdown voltage in field plated Ga<sub>2</sub>O<sub>3</sub> MOSFET," in *Proc. 76th Device Res. Conf. (DRC)*, Jun. 2018, pp. 1–2.
- [20] Z. Hu *et al.*, "Enhancement-mode Ga<sub>2</sub>O<sub>3</sub> vertical transistors with breakdown voltage >1 kV," *IEEE Electron Device Lett.*, vol. 39, no. 6, pp. 869–872, Jun. 2018.
- [21] W. Li, K. Nomoto, Z. Hu, T. Nakamura, D. Jena, and H. G. Xing, "Single and multi-fin normally-off Ga<sub>2</sub>O<sub>3</sub> vertical transistors with a breakdown voltage over 2.6 kV," in *IEDM Tech. Dig.*, Dec. 2019, p. 12.
- [22] T. P. Chow, I. Omura, M. Higashiwaki, H. Kawarada, and V. Pala, "Smart power devices and ICs using GaAs and wide and extreme bandgap semiconductors," *IEEE Trans. Electron Devices*, vol. 64, no. 3, pp. 856–873, Mar. 2017.
- [23] Y. Q. Huang *et al.*, "Structural and photoelectrical properties of Ga<sub>2</sub>O<sub>3</sub>/SiC/Al<sub>2</sub>O<sub>3</sub> multilayers," *J. Alloys Compounds*, vol. 717, pp. 8–13, Sep. 2017.
- [24] J. C. Yang *et al.*, "Vertical geometry 33.2 A, 4.8 MW cm<sup>2</sup> Ga<sub>2</sub>O<sub>3</sub> field-plated Schottky rectifier arrays," *Appl. Phys. Lett.*, vol. 114, no. 23, Jun. 2019, Art. no. 232106.
- [25] S. Ahn, F. Ren, L. Yuan, S. J. Pearton, and A. Kuramata, "Temperature-dependent characteristics of Ni/Au and Pt/Au Schottky diodes on  $\beta$ -Ga<sub>2</sub>O<sub>3</sub>," *ECS J. Solid State Sci. Technol.*, vol. 6, no. 1, pp. P68–P72, 2017.
- [26] S. Oh, G. Yang, and J. Kimz, "Electrical characteristics of vertical Ni/ $\beta$ -Ga<sub>2</sub>O<sub>3</sub> Schottky barrier diodes at high temperatures," *ECS J. Solid State Sci. Technol.*, vol. 6, no. 2, pp. Q3022–Q3025, 2017.
- [27] D. Splith *et al.*, "Determination of the mean and the homogeneous barrier height of Cu Schottky contacts on heteroepitaxial  $\beta$ -Ga<sub>2</sub>O<sub>3</sub> thin films grown by pulsed laser deposition," *Phys. Status Solidi (A)*, vol. 211, no. 1, pp. 40–47, Jan. 2014.
- [28] T. Oshima *et al.*, "Electrical properties of Schottky barrier diodes fabricated on (001)  $\beta$ -Ga<sub>2</sub>O<sub>3</sub> substrates with crystal defects," *Jpn. J. Appl. Phys.*, vol. 56, no. 8, Aug. 2017, Art. no. 086501.
- [29] Y. Yao, R. Gangireddy, J. Kim, K. K. Das, R. F. Davis, and L. M. Porter, "Electrical behavior of  $\beta$ -Ga<sub>2</sub>O<sub>3</sub> Schottky diodes with different Schottky metals," *J. Vac. Sci. Technol. B*, vol. 35, no. 3, May 2017, Art. no. 03D113.
- [30] Q. M. He *et al.*, "Schottky barrier diode based on  $\beta$ -Ga<sub>2</sub>O<sub>3</sub> (100) single crystal substrate and its temperature-dependent electrical characteristics," *Appl. Phys. Lett.*, vol. 110, no. 9, Feb. 2017, Art. no. 093503.
- [31] C. Fares, F. Ren, and S. J. Pearton, "Temperature-dependent electrical characteristics of  $\beta$ -Ga<sub>2</sub>O<sub>3</sub> diodes with W Schottky contacts up to 500° C," *ECS J. Solid State Sci. Technol.*, vol. 8, pp. Q3007–Q3012, Jan. 2019.
- [32] J. C. Yang *et al.*, "Switching behavior and forward bias degradation of 700V, 0.2 A,  $\beta$ -Ga<sub>2</sub>O<sub>3</sub> vertical geometry rectifiers," *ECS J. Solid State Sci. Technol.*, vol. 8, pp. Q3028–Q3033, Jan. 2019.
- [33] T.-H. Yang *et al.*, "Temperature-dependent electrical properties of  $\beta$ -Ga<sub>2</sub>O<sub>3</sub> Schottky barrier diodes on highly doped single-crystal substrates," *J. Semicond.*, vol. 40, no. 1, 2019, Art. no. 012801.
- [34] M. Pavesi *et al.*, " $\epsilon$ -Ga<sub>2</sub>O<sub>3</sub> epilayers as a material for solar-blind UV photodetectors," *Mater. Chem. Phys.*, vol. 205, pp. 502–507, Feb. 2018.
- [35] T.-H. Yang *et al.*, "Temperature-dependent electrical properties of  $\beta$ -Ga<sub>2</sub>O<sub>3</sub> Schottky barrier diodes on highly doped single-crystal substrate," *J. Semicond.*, vol. 40, no. 1, Jan. 2019, Art. no. 012801.
- [36] J. Kuzmík, D. Pogany, E. Gornik, P. Javorka, and P. Kordoš, "Electrical overstress in AlGaIn/GaN HEMTs: Study of degradation processes," *Solid-State Electron.*, vol. 48, no. 2, pp. 271–276, Feb. 2004.
- [37] L.-B. Chang *et al.*, "High ESD reliability InGaIn light emitting diodes with post deposition annealing treated ZnO films," *Solid-State Electron.*, vol. 77, pp. 77–81, Nov. 2012.
- [38] C.-T. Lee, H.-P. Shiao, N.-T. Yeh, C.-D. Tsai, Y.-T. Lyu, and Y.-K. Tu, "Thermal reliability and characterization of InGaP Schottky contact with Ti/Pt/Au metals," *Solid-State Electron.*, vol. 41, no. 1, pp. 1–5, Jan. 1997.
- [39] Z. Islam, A. Haque, and N. Glavin, "Real-time visualization of GaN/AlGaIn high electron mobility transistor failure at off-state," *Appl. Phys. Lett.*, vol. 113, no. 18, Oct. 2018, Art. no. 183102.
- [40] B. Wang *et al.*, "In situ transmission electron microscopy of transistor operation and failure," *Nanotechnology*, vol. 29, no. 31, Aug. 2018, Art. no. 31LT01.
- [41] Z. Islam *et al.*, "Heavy ion irradiation effects on GaN/AlGaIn high electron mobility transistor failure at off-state," *Microelectron. Rel.*, vol. 102, Nov. 2019, Art. no. 113493.
- [42] M. A. Haque and M. T. A. Saif, "Deformation mechanisms in free-standing nanoscale thin films: A quantitative in situ transmission electron microscope study," *Proc. Nat. Acad. Sci. USA*, vol. 101, no. 17, pp. 6335–6340, Apr. 2004.
- [43] M. Kiritani, "Similarity and difference between fcc, bcc and hcp metals from the view point of point defect cluster formation," *J. Nucl. Mater.*, vol. 276, nos. 1–3, pp. 41–49, Jan. 2000.
- [44] Y. Matsukawa and S. J. Zinkle, "One-dimensional fast migration of vacancy clusters in metals," *Science*, vol. 318, no. 5852, pp. 959–962, Nov. 2007.
- [45] S. Gao, Y. Q. Wu, R. K. Kang, and H. Huang, "Nanogrinding induced surface and deformation mechanism of single crystal  $\beta$ -Ga<sub>2</sub>O<sub>3</sub>," *Mater. Sci. Semicond. Process.*, vol. 79, pp. 165–170, Jun. 2018.
- [46] M. H. Wong, K. Sasaki, A. Kuramata, S. Yamakoshi, and M. Higashiwaki, "Field-plated Ga<sub>2</sub>O<sub>3</sub> MOSFETs with a breakdown voltage of over 750 V," *IEEE Electron Device Lett.*, vol. 37, no. 2, pp. 212–215, Feb. 2016.
- [47] B. Wang *et al.*, "In situ transmission electron microscopy of transistor operation and failure," *Nanotechnology*, vol. 29, May 2018, Art. no. 31LT01.